Micromechanical Modeling of Discontinuous Shear Thickening in Granular Media-Fluid Suspension

Daniel H. Johnson[a], Farshid Vahedifard[b], Bohumir Jelinek[c], John F. Peters[d]

[a] Dept. of Mechanical Engineering and Center for Advanced Vehicular Systems (CAVS), Mississippi State University, Mississippi State, MS 39762, USA. email: dhj21@cavs.msstate.edu

[b] Corresponding author, Dept. of Civil and Environmental Engineering and Center for Advanced Vehicular Systems (CAVS), Mississippi State University, Mississippi State, MS 39762, USA. email: farshid@cee.msstate.edu

[c] Center for Advanced Vehicular Systems (CAVS), Mississippi State University, Mississippi State , MS 39762, USA, email: bj48@cavs.msstate.edu

[d] Center for Advanced Vehicular Systems (CAVS), Mississippi State University, Mississippi State, MS 39762, USA, email: john@cavs.msstate.edu

Abstract

Shear thickening in a fluid occurs when the viscosity of the fluid increases with increasing applied strain rate. When the rise in viscosity occurs by orders of magnitude, the fluid undergoes discontinuous shear thickening, which can be devastating in industrial applications. We present a particle-scale numerical technique that can simulate these phenomena. By coupling the discrete element method (DEM) and lattice Boltzmann method (LBM), we developed a micromechanical model that can simulate the inter-particle stresses for particles that are immersed in a fluid. A comparison of the simulation results against experimental results reported in the literature demonstrates the potential of the method as a research tool. The comparison included parametric studies to investigate the effects of solid fraction, particle-particle, and particle-wall contact stiffness. With a systematic variation of the wall stiffness, the DEM-LBM model demonstrates that increasing boundary stiffness directly increases the maximum shear

stress of the shear thickening regime. For the case of particles settling at low stresses, the DEM-LBM model has the advantage of providing insight into particle-scale interactions in a detail not possible using a continuum method based on phenomenological constitutive equations.We also show that the central mechanism creating the shear thickening is the dilation of the particulate media per traditional soil mechanics principles.

Keywords: Shear thickening fluid; Numerical modeling; Discrete Element Method; Lattice Boltzmann; dilation; Fluid Suspension.

1. Introduction

Shear thickening in a fluid occurs when the viscosity of the fluid increases as the applied shear stress or strain rate increases. Shear thickening is often observed in colloidal dispersions and densely packed suspensions [1-9]. At specific strain rate levels, the jump in viscosity can be discontinuous and quite dramatic. Shear thickening materials are important in the fields of shock absorption and dampers. These types of materials have been used to increase body armor strength and energy absorption [10]. The drastic increase in resistance leads to problems in industrial processing, such as jamming in extrusion through small openings [7]. Shear thickening can be masked by a yield stress increase caused by particle surface interactions, electric and magnetic fields, and boundary confinement [11].

The shear thickening can appear in continuous, inertial, and discontinuous form. Continuous shear thickening describes the increase in viscosity at low particle packing fractions, φ, and is generally mild, with only a few percent increase in viscosity [2,12]. Inertial shear thickening, observable even in simple Newtonian fluids such as water, occurs when the strain rate is increased to very high values, and the increase in viscosity does not strongly depend on the solid fraction. Discontinuous shear thickening (DST) happens when the viscosity of the system suddenly increases by orders of magnitude with increasing stress. The transition from continuous to discontinuous shear thickening for non-Brownian suspensions is an important but not well-understood phenomenon [13]. Peters *et al.* [14] investigated the relationship between shear jamming and the onset of DST. An example of this type of shear thickener is a cornstarch-water mixture [3].

Recently, several experimental or numerical studies observed and investigated shear thickening (e.g., [3,5-6,8-9]). Brown and Jaeger [3] completed experiments showing the effects and behaviors of discontinuous shear thickening. DST occurs at a stress range that is mostly independent of solid packing fraction, φ [15]. The sudden increase of viscosity only occurs once φ reaches 0.5 for nearly spherical particles [16], and DST is generally reversible. Important phenomena involved in DST include force chain formation and dilation. Force chains are discrete chainlike particle groups that carry the stronger normal contact forces and tend to align along principal stress trajectories [17-18]. Under simple shear conditions such as in shear bands or at the steady state condition in a parallel plate rheometer, the force chains create groups of jammed particles that transmit forces in direction corresponding to the applied shear [19]. When a granular material is sheared, the particles must move around each other and take up more volume than when settled, resulting in dilation [3].

Modeling of DST has focused in the areas of colloidal dispersions[2]. Other continuum-based models using phenomenological constitutive equations have been used to model DST [3,20]. Bian *et al.* [21] used smooth particle hydrodynamics to simulate the behavior of a suspension of particles. However, continuum modeling of DST poses a complex solid-fluid interaction problem, the physics of which is better suited to discrete simulations of interparticle interactions in micro-scale. Recent work has been done on modeling DST with contact laws, such as the DEM, that include a hydrodynamic force term, which models the fluid phase [4,8,22]. Mari *et al*. [9] modeled shear thickening for Brownian suspensions by using a model that included contact laws, hydrodynamic lubrication forces, repulsive forces, and Brownian forces. However, these recent models do not model the fluid as a separate phase. To the authors' knowledge, such a micromechanical multiphase model has not been developed in any of the previous studies of shear thickening fluids.

To model both phases independently, we have developed a numerical model by coupling the DEM with the LBM to investigate DST mechanics at the particle scale. The DEM is used to locally and discretely solve the inter-particle interactions, whereas the LBM calculates the hydrodynamic contribution of the fluid. The DEM-LBM model creates a micromechanical model that can locally determine the inter-particle interactions and fluid-particle interaction to globally reproduce the observed shear thickening behavior. Instead of using an averaged effect of the particle interactions, interactions among particles are treated discretely. The potential of the proposed numerical model is demonstrated by comparison with the parallel plate rheometry experiment by Brown and Jaeger [3]. The DEM-LBM model is used to predict the viscosity of the system being sheared. The simulation is performed over a range of shear stresses to capture the stress scale, and for a different number of packing fractions to observe the discontinuity in bulk viscosity as the shear rate is increased. Other parameters such as particle-wall contact stiffness and inter-particle friction are also studied to determine their impact on dilative behavior. Previous modeling efforts have shown the effects of solid fraction and particle friction [4-6]. Although the experimental tests reported by Brown and Jaeger [3] showed that increasing boundary stiffness would increase the maximum shear stress that exhibits shear thickening, the current DEM-LBM modeling is the first, to the authors' knowledge, to present this phenomenon with a systematic variation of the wall stiffness.

2. Formulation and Implementation of the DEM-LBM Model

In recent years, coupling the DEM and the LBM has become a well-established method for solving many fluid-particle interaction problems in geomechanics (e.g., [23-26]). In this coupled method, the DEM resolves the inter-particle interactions, and the LBM solves the Navier-Stokes equations for fluid flow. Feng et al. [23] used the DEM-LBM to model a vacuum dredging system for mineral recovery, where particles were pulled through a suction pipe at turbulent Reynolds numbers. Lomine et al. [24] used the DEM-LBM to model piping erosion. In these simulations, 2D discs were placed in a rectangular domain, and a pressure gradient was applied to cause the flow of the fluid. The DEM-LBM is useful because both methods are local and employ explicit time integration, making them particularly suitable for parallelization [27].

The following sections briefly discuss the DEM and LBM formulations, boundary conditions, and coupling between the DEM and LBM which were used in this study. In general, the LBM calculates the forces exerted on the solid boundary by the fluid and passes the information to the DEM. Then, the DEM uses the total force on the solid boundary to integrate the equations of motion for the solid particles.

2.1. Discrete Element Method

The DEM is a robust numerical method that was originally developed by Cundall and Strack [28] to simulate dry granular materials. Since then, the method and its subsequent developments have been extensively used for simulating various problems in geomechanics. The DEM treats particles as distinct interacting bodies that are governed locally by contact laws that control particle interpenetration and dissipate energy. These contact laws can be determined by independent laboratory investigations as described by Cole and Peters [29]. An example of a contact law is the power law model that is evaluated for contact overlap [30] and is written as:

$$F_N = K_N \delta_n^m \tag{1}$$

where m=1 for the linear contact law, and m is a power law parameter for the power law model. K_N is the normal stiffness and δ is the penetration distance. In this study, simple linear contact laws are used, but with differing moduli for loading and unloading to represent the energy dissipation.

After determining the contact forces on each particle, the particle velocity and angular rotation are determined by integrating Newton's equations of motion. The equations of motion are expressed as:

$$m \frac{\partial v_i}{\partial t} = m g n_i^g + \sum_{c=1}^{N_c} f_i^c + F_F \tag{2}$$

and

$$I_m \rho \, \frac{\partial \omega_i}{\partial t} = \sum_{c=1}^{N_c} e_{ijk} f_j^c r_k^c + \sum_{c=1}^{N_c} M_i^c + T_F, \tag{3}$$

where m and I_m are the particle mass and moment of inertia respectively, $g n_i^g$ the acceleration of gravity, f_i^c and M_i^c the forces and moments applied at the contacts, F_F and T_F are the hydrodynamic force and torque, respectively, and N_c the number of contacts for the particle. The third term in Equation 3 represents the contribution of rolling resistance to model the effects of shape for non-spherical particles [18]. However for the STF simulations, spherical particles were modeled, and this term is equal to zero. Following Peters *et al*. [17], the particle stress tensor and the average continuum stress in the solid fraction are defined as:

$$\sigma_{ij}^{p} = \frac{1}{V_p} \sum_{c=1}^{N^c} f_i^c r_j^c \tag{4}$$

$$\bar{\sigma}_{ij} = \frac{1}{V} \sum_{p=1}^{N^p} V_p \sigma_{ij}^{p} = \frac{V_s}{V} \langle \sigma_{ij}^{p} \rangle \tag{5}$$

where V is the total volume, V_p is the volume of each particle, V_s is the total particle volume, N^c is the number of contacts, N^p is the number of particles, f_i^c is the ith component of the force acting at the contact, r_j^c is the jth component of the radius vector from the center of the particle to the contact. The particle stresses are useful for identifying the particles transmitting higher than average loads through force chains. The principal stresses of each particle are calculated by finding the eigenvalues of the stress tensor. When showing force chains, the maximum (compressive) value of the principal stresses is used. The average continuum stress is useful for investigating the stress history of the system in the form of a stress path plot of the intergranular stress, p, and the deviatoric stress, q, which are defined as:

$$p = \frac{S_1 + S_2 + S_3}{3} \tag{6}$$

$$q = \frac{1}{\sqrt{2}} \sqrt{(S_1 - S_2)^2 + (S_1 - S_3)^2 + (S_2 - S_3)^2} \tag{7}$$

where S_1 , S_2, and S_3 are the principal stresses of the average stress tensor. In the following sections, the soil mechanics convention of taking compression as positive is used. Thus, when dilation occurs it is a negative volume change that will produce a positive boundary stress which is compressive.

2.2. Lattice Boltzmann Method

The LBM is a simulation technique commonly used for solving fluid flow and transport equations (*e.g.,* [31-33]). The LBM is developed based on Boltzmann's equation [34], which was derived from the gas kinetic theory. In this method, a collision operator is employed to describe the time and spatial evolution of a distribution function of particles. Boltzmann's equation has a direct relationship with the Navier–Stokes equations [35]. The LBM characterizes the fluid at points located on a regular *d*-dimensional lattice. For a lattice representation D*d*Q*z*, each point in the *d*-dimensional lattice links to neighboring points with *z* links that correspond to velocity directions. For example, the D3Q15 lattice in three dimensions uses fifteen velocity vectors $\boldsymbol{e}_{\mathbf{0}}$ to $\boldsymbol{e}_{\mathbf{14}}$, as shown in Figure 1.

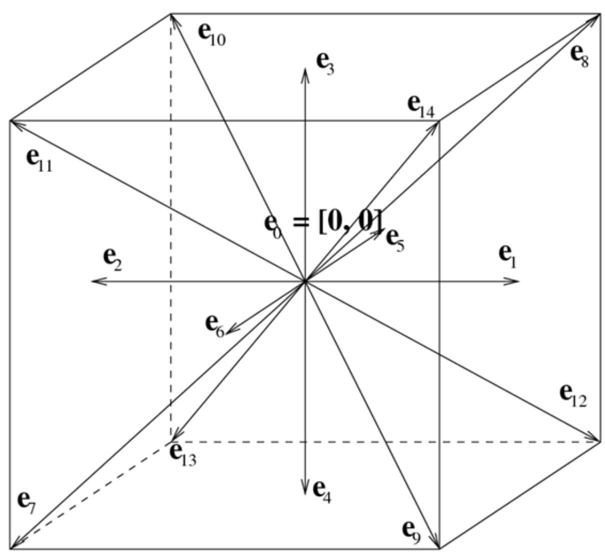

Figure 1. D3Q15 lattice velocities. Lattice velocities e_5 and e_6 are positive and negative in the z-direction, respectively.

2.2.1 Density distribution functions and their time evolution

The primary variable of the LBM is the density distribution function f_i. For the D3Q15 lattice shown in Figure 1, density distribution functions f_0 to f_{14}, corresponding to velocity vectors $\boldsymbol{e}_{\mathbf{0}}$ to $\boldsymbol{e}_{\mathbf{14}}$, represent portions of a local mass density moving into neighboring cells in the directions of discrete velocities. The macroscopic fluid density ρ at each lattice point is a sum of the distribution functions at that lattice point:

$$\rho = \sum_{i=0}^{14} f_i \tag{8}$$

Fluid velocity at the lattice point is a weighted sum of lattice velocities, with distribution functions being the weight coefficients:

$$u = \frac{\sum_{i=0}^{14} f_i e_i}{\sum_{i=0}^{14} f_i} = \frac{\sum_{i=0}^{14} f_i e_i}{\rho} \tag{9}$$

where f_i/ρ ratio can be interpreted as a probability of finding a particle at a given spatial location with a discrete velocity $\boldsymbol{e_i}$.

Using the collision model of Bhatnagar-Gross-Krook (BGK, [36]) with a single relaxation time, the time evolution of the distribution functions is given by

$$f_i(r + e_i\Delta t, t + \Delta t) = f_i(r, t) + \frac{1}{\tau_u}\left(f_i^{eq}(r, t) - f_i(r, t)\right), i = 0 \ldots 14 \tag{10}$$

where $\boldsymbol{r}$ and t are the space and time position of a lattice site, Δt is the time step, and τ_u is the relaxation parameter for the fluid flow. The relaxation parameter τ_u specifies how fast each density distribution function f_i approaches its equilibrium f_i^{eq}. Kinematic viscosity, ν, is related to the relaxation parameter, τ_u, the lattice spacing, Δx, and the simulation time step, Δt, by

$$\nu = \frac{\tau_u - 0.5}{3}\frac{\Delta x^2}{\Delta t} \tag{11}$$

Depending on the dimensionality d of the modeling space and a chosen set of the discrete velocities $\boldsymbol{e_i}$, the corresponding equilibrium density distribution function can be found [37]. For the D3Q15 lattice, the equilibrium distribution functions f_i^{eq} are

$$f_i^{eq}(r) = \omega_i \rho(r)\left(1 + 3\frac{e_i \cdot u(r)}{c^2} + \frac{\frac{9}{2}\left(e_i \cdot u(r)\right)^2}{c^4} - \frac{\frac{3}{2}u(r) \cdot u(r)}{c^2}\right) \tag{12}$$

with the lattice velocity $c=\Delta x/\Delta t$ and the weights

$$\omega_i = \begin{cases} \frac{2}{9} & i = 0 \\ \frac{1}{9} & i = 1 \dots 6 \\ \frac{1}{72} & i = 7 \dots 14 \end{cases} \tag{13}$$

Using the expansion proposed by Chapman and Cowling [38], it can be shown that LBM Eqs. 8 to 13 provide an approximation of the incompressible Navier-Stokes Eqs. 14 to 15 without external forces:

$$\rho\left[\frac{\partial u}{\partial t} + u \cdot \nabla u\right] = \nabla \cdot (\mu \nabla \mathrm{u}) \tag{14}$$

$$\nabla \cdot u = 0 \tag{15}$$

where the $\mu=\nu\rho$ is the dynamic viscosity of fluid. This approximation is valid in the limit of low Mach number $M=|u|/c_s$, where $c_s = c/\sqrt{3}$ is the lattice speed of sound.

2.2.2 Immersed moving boundary

The immersed moving boundary (IMB) technique [30, 39-40] allows solid boundaries to move through the computational grid. The IMB method introduces a subgrid resolution at the solid-liquid boundaries, resulting in smoothly changing forces and torques exerted by the fluid on moving particles. The IMB introduces an additional collision operator $\mathbf{\Omega}_i^S$ expressing collisions of solid particles with fluid as

$$\Omega_i^S = f_{-i}(r,t) - f_i(r,t) + f_i^{eq}(\rho, U_S) - f_{-i}^{eq}(\rho, u) \tag{16}$$

The time evolution of the density distribution functions in IMB includes $\mathbf{\Omega}_i^S$

$$f_i(r + e_i\Delta t, t + \Delta t) = f_i(r,t) + [1 - \beta(\epsilon,\tau)]\frac{1}{\tau}\left(f_i^{eq}(r,t) - f_i(r,t)\right) + \beta(\epsilon,\tau)\Omega_i^S \qquad i = 0, 1, \ldots, 14 \tag{17}$$

where the weighting factor $\beta(\varepsilon,\tau)$ depends on solid coverage ε and relaxation parameter τ

$$\beta(\epsilon,\tau) = \frac{\epsilon}{1 + \dfrac{1-\epsilon}{\tau - 0.5}} \tag{18}$$

2.2.3 Fluid force and torque

The total hydrodynamic force exerted by the fluid on a particle is calculated by summing the momentum change at every lattice cell due to the new collision operator:

$$\boldsymbol{F}_F = \frac{\Delta x^3}{\Delta t}\sum_n\left(\beta_n\sum_{i=0}^{14}\mathbf{\Omega}_i^S\boldsymbol{e}_i\right) \tag{19}$$

and the total hydrodynamic torque can then be calculated by:

$$\boldsymbol{T}_F = \frac{\Delta x^3}{\Delta t}\sum_n(\boldsymbol{r}_n - \boldsymbol{r}_c)\times\left(\beta_n\sum_{i=0}^{14}\mathbf{\Omega}_i^S\boldsymbol{e}_i\right) \tag{20}$$

where $\mathbf{r}_n - \mathbf{r}_c$ is the vector from the center of the particle to the center of the lattice cell.

It should be noted that the current DEM-LBM model does not explicitly account for lubrication forces, so the LBM does not resolve the detailed particle-fluid-particle interactions for small gaps. Feng and Michaelides [41] resolved this phenomenon by applying a strong repulsive force if the gap between two particles becomes smaller than a given threshold value. Alternatively, a “buffer zone” can be introduced at the location of the DEM contacts, where the contact radius is marginally larger than the physical radius, and the effects of nodal conflicts can be minimized [30]. Nevertheless, the DEM-LBM model presented here shows good agreement with experimental data, suggesting that the effect of lubrication force in the corresponding physical experiment can be considered negligible, although considerable study remains to be done on lubrications effects.

2.3 Coupled DEM-LBM

The LBM time step Δt is determined from the kinematic viscosity of fluid v, required grid resolution Δx, and constraints on the relaxation parameter (τ>0.5) according to Eq. 11. The relaxation parameter must be chosen low enough to achieve a sufficient time resolution. An upper limit on the relaxation parameter is given by the low Mach number constraint. For DEM, the largest acceptable time step value is determined from the smallest particle mass m_i and the stiffest spring k_i in the system, given the frequency of fastest oscillations

$$\omega_{max} = \sqrt{\frac{MAX(k_i)}{MIN(m_i)}} \tag{21}$$

and their time period

$$T_{min} = \frac{2\pi}{\omega_{max}} \tag{22}$$

In this work, the LBM time step is constrained to be greater than or equal to the DEM time step. Accordingly, the LBM time step is determined first, and then the DEM time step is adjusted to perform an integer number of substeps before performing the LBM calculation. During the DEM subcycling, the fluid forces and torques remain constant, and the fluid-solid boundary does not move. Therefore, care must be taken when deciding the number of DEM subcylces [30]. The DEM integrates the equations of motion, using the Velocity Verlet method. The sub-cycling process and updating of forces for each method can be seen in Figure 2.

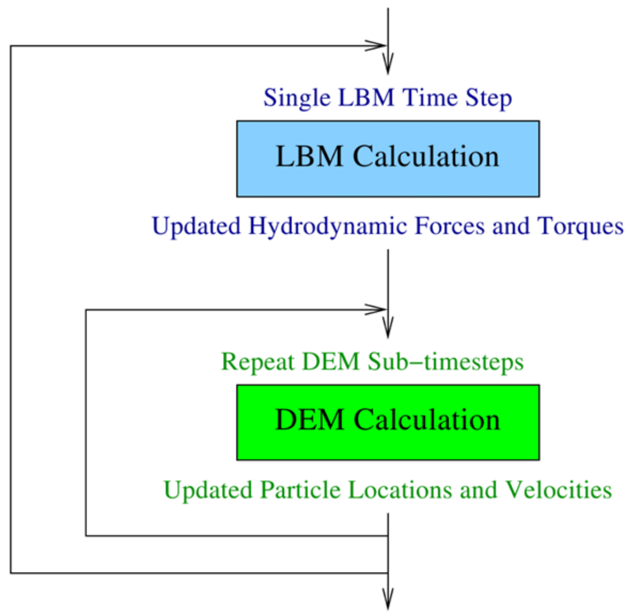

Figure 2. Diagram showing the sub-cycling process and updating of particle forces between the DEM and LBM.

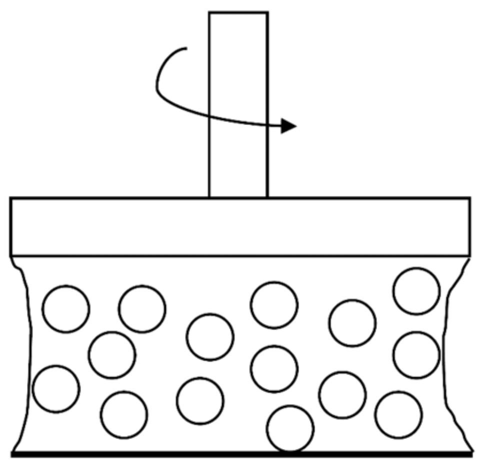

Figure 3. Experimental setup of a standard parallel plate rheometer.

The DEM-LBM simulations completed in this study were performed on the Shadow cluster at the Mississippi State University High Performance Computing Collaboratory. The LBM portion of the algorithm was parallelized using spatial domain decomposition algorithm, as described in [27]. Average computational time for the simulation utilizing 128 Intel Xeon E5-2680 v2 processor cores was 72 hours.

3. Numerical Simulation of Shear Thickening and Validation

To investigate the validity of the proposed numerical model for simulating shear thickening, the results from the DEM-LBM model are compared against experimental results reported by Brown and Jaeger [3]. As shown in Figure 3, the experiments of Brown and Jaeger [3] were performed using a parallel plate rheometer. A shear stress, or strain rate, was applied to the top plate, which caused the shearing motion, and the global resistance of the system was measured using the following equation,

$$\eta = \frac{\tau}{\dot{\gamma}} \tag{23}$$

where η is the viscosity or mechanical resistance, τ is the shear stress, and $\dot{\gamma}$ is the strain rate. A stress above the shear-thickening domain was applied for at least 100 s, and then the stress was ramped down to the desired value. To reach a steady state, a ramp rate of 500 s per decade of stress was used. By measuring the velocity of the plate, the global viscosity of the system was calculated by Equation 23.

Brown and Jaeger [3] completed experiments for different particle sizes, solid fractions, and fluid types. For the DEM-LBM simulations, the 150 μm ZrO_2 spheres immersed in mineral oil with a gap length of 890 μm and solid fraction, φ, of 0.53 was studied. By knowing the solid fraction, gap height, and particle radius, the number of particles was calculated. To create an initial configuration, the particles were first loosely packed, compressed to final dimensions, and allowed to settle to gravity. A sufficient amount of time was simulated to allow the damping of particle velocities to very small values. After achieving the stable initial configuration, the desired shear stress was applied to the top wall with the velocity of the wall being calculated by the DEM-LBM model. Spikes in the velocity profile due to random instabilities of particle contacts were smoothed out by time averaging before the viscosity values were calculated.

Most of the parameters used in the DEM-LBM model were specified by the experimental data reported by Brown and Jaeger [3] and can be seen in Table I. The DEM parameters in Table II were not explicitly available from experimental data, so the initial values of these parameters were chosen by calibrating the model with the experimental data for the largest values of applied stress. The LBM parameters such as lattice spacing and relaxation parameter were chosen as reasonable values for the simulations. For example, the relaxation parameter must be above 0.5 and low enough that the simulation is stable. The grid spacing was chosen in order to provide an accurate enough representation of the spherical particle boundary. The particle normal stress, particle shear stress, and coefficient of restitution parameters were chosen so that particles behaved reasonably, without large overlap when in contact. The remaining parameters were adjusted to fit the experimental data. The effects of these parameters will be examined. Initial values for parameters such as wall stiffness, particle friction coefficient, and wall friction coefficient were discussed by Brown and Jaeger [3]. The experimental data suggested that it was unnecessary to account for polydispersity, thus all particles in the DEM-LBM model have the same radius. However, the value for the wall stiffness parameter was difficult to initialize; therefore, trial and error calibration was used to best fit the experimental data for the highest values of applied stress. Not knowing an appropriate starting value for the boundary stiffness led to the parametric study for wall stiffness. The effects of varying the wall-particle stiffness and particle-particle friction terms are examined in the parametric study. The results were most sensitive to changes in these two parameters.

Table 1. Input parameters from the shear thickening experiment (data from [3]).

Property	Units	Value
Particle Radius	μm	75

Particle Density	kg/m^3	3900
Gap Height	μm	890
Fluid Viscosity	Pa-s	0.058
Fluid Density	kg/m^3	870
Solid fraction	---	0.53

Table 2. Input parameters used in the DEM-LBM model

Property	Units	Value
Particle Normal Stiffness	N/m	1000
Particle Shear Stiffness	N/m	200
Coefficient of Restitution	---	0.2
Particle-Particle Friction	---	0.8
Wall Normal Stiffness	N/m	0.5
Wall Shear Stiffness	N/m	0.1
Wall-Particle Friction	---	0.8
Relaxation Parameter	---	0.9
Lattice Spacing	μm	18.5

The total volume of the system was established by setting the length of the loading direction to four times the gap height to avoid correlation effect from the periodic boundary condition. The depth of the system was set equal to the gap height. The number of simulated particles was 845. The LBM grid dimensions were 192×50×48 for the loading, gap height, and the depth direction, respectively. These grid dimensions impose 8 lattice cells per particle diameter. The gap height included two more cells for the walls.

For the DEM-LBM model, the following approximations were used to simplify the model. The periodic boundary conditions were applied in the loading direction (x-axis) and in the thickness direction (z-axis), what is reasonable as long as the diameter of the plate is large relative to its height. By using periodic boundaries, the end effects, such as surface tension or solid wall confinement are assumed to be negligible. Also, the fluid phase for the suspension was assumed to behave as a Newtonian fluid. From the experimental data, the Reynolds number was always kept below 100 to avoid inertial effects. A no slip boundary condition is applied for the fluid flow at all particles boundaries and the wall boundaries. The experimental setup shown in Figure 3 was modeled with a rectangular domain with dimensions of 3.56 mm, 0.89 mm, and 0.89 mm representing the x, y, and z-directions. The geometry and boundary conditions for the DEM-LBM model can be seen in Figure 4.

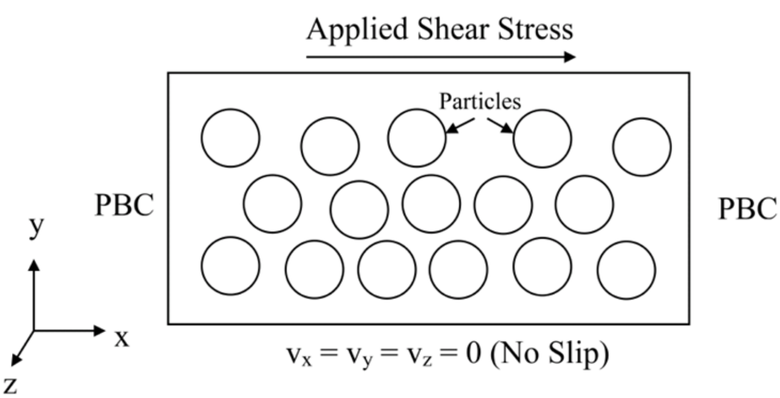

Figure 4. Boundary conditions used for the DEM-LBM model. As shown, the top wall has an applied shear stress boundary condition, the bottom wall is fixed. Periodic boundary conditions (PBC) are applied in both x and z-directions. Both the top and bottom wall are flat plates with a friction parameter of 0.8. The LBM splits the domain into 192×50×48 lattice points in x,y, and z-directions.

To fully evaluate the DEM-LBM model, several values of applied shear stress were chosen to span the range of the experimental data. The selected values were 0.1 Pa, 0.3 Pa, 1 Pa, 3 Pa, 10 Pa, and 30 Pa. The DEM-LBM data are plotted against the experimental data showing a very good agreement, as seen in Figure 5. Each applied stress was simulated for 1.5 s, which was sufficient for each plate velocity to approach a steady state value. As an example, Figure 6 plots the plate velocity versus time for the applied stress of 10 Pa. The velocity used to determine the apparent viscosity of the system was obtained by time averaging.

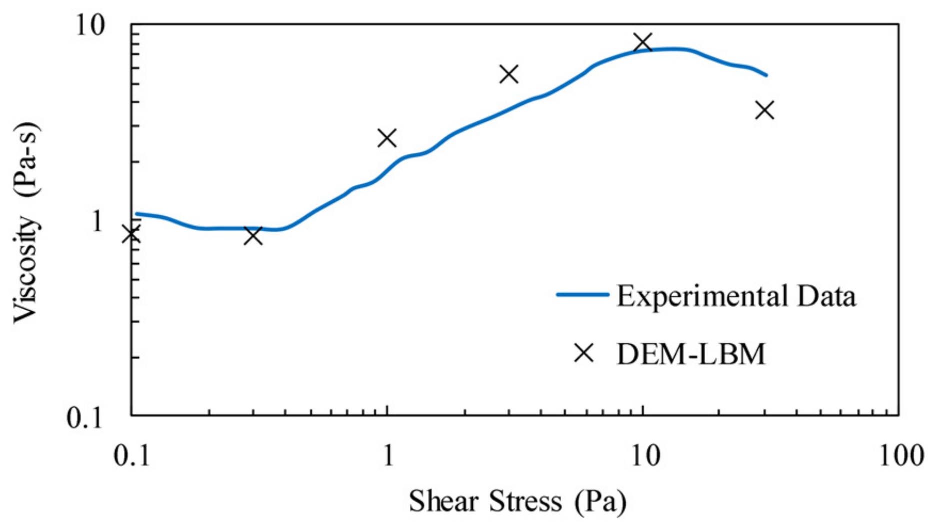

Figure 5. Viscosity-stress plot comparing the DEM-LBM results to the experimental data.

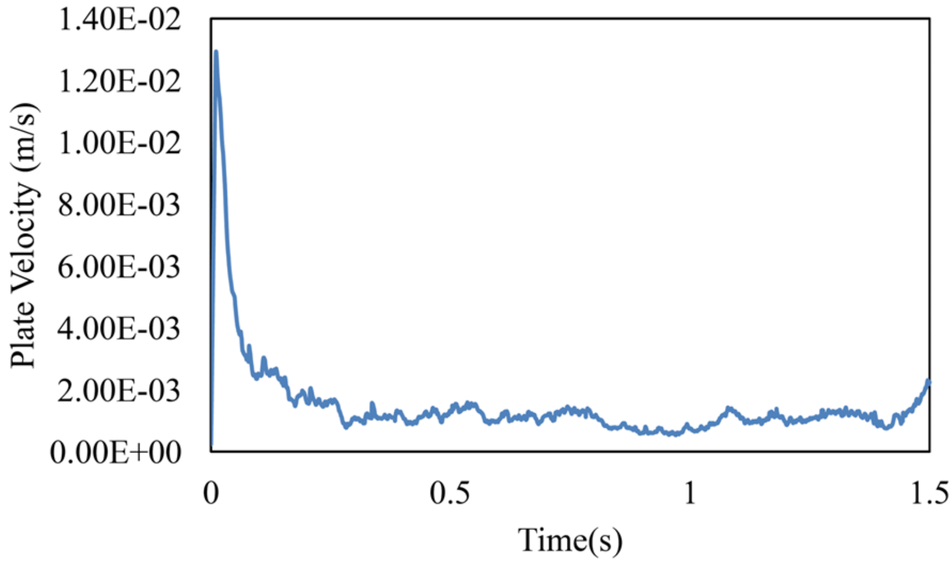

Figure 6. Plate velocity versus time for an applied stress of 10 Pa.

Shear profiles were generated for each applied stress as seen in Figure 7 and compared to some experimental values [3] in Figure 8. These profiles were generated by plotting the average particle velocity as a function of the distance from the plate.

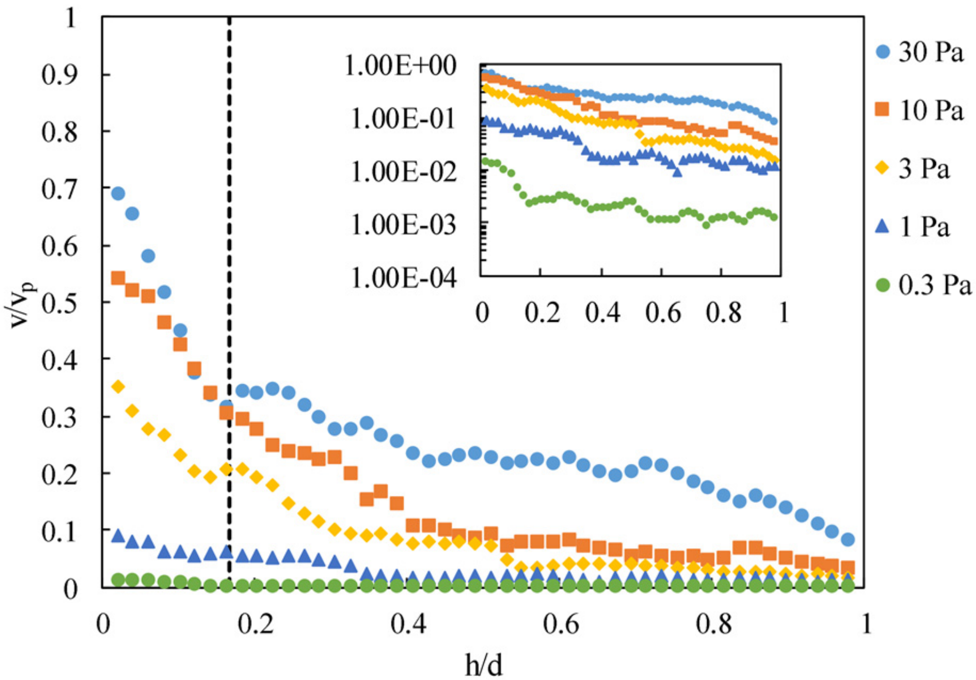

Figure 7. Shear profile for all applied stresses. The particle velocity, v, was normalized by the plate velocity, v_p, and the distance from the plate, h, was normalized by the gap width, d. The vertical dashed line shows the distance of 1 particle diameter. A log-linear plot is shown in the top right corner.

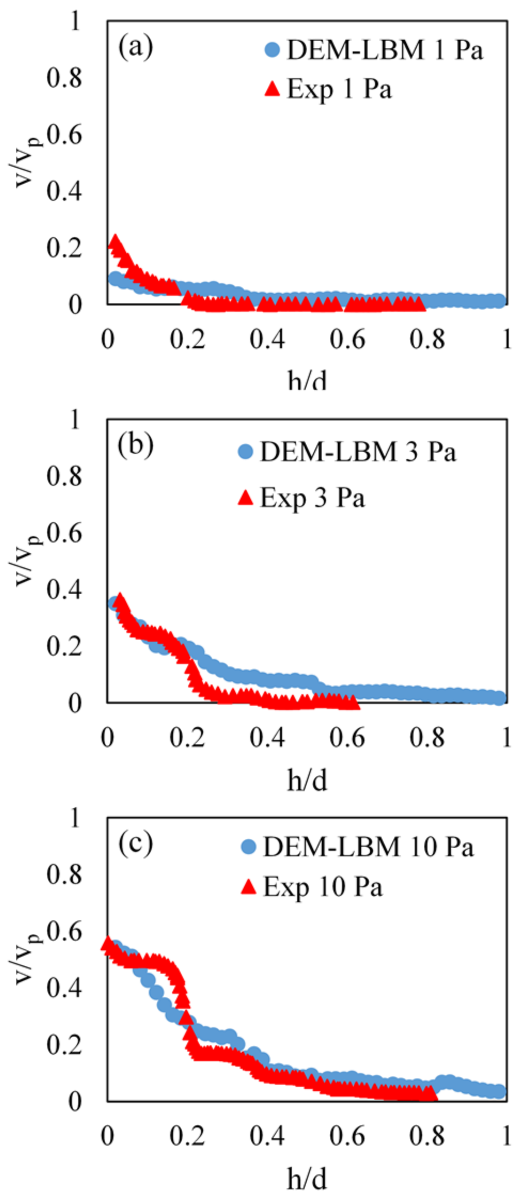

Figure 8. Comparison of shear profiles at applied stress levels of a) 1 Pa, b) 3 Pa, and c) 10 Pa. The particle velocity, v, was normalized by the plate velocity, v_p, and the distance from the plate, h, was normalized by the gap width, d. The experimental data is from [3].

The effect of dilation on the system is illustrated in Figure 9, which shows the normal and shear stresses on the moving wall from both the fluid phase and the solid phase. The figure demonstrates that at the beginning of the simulation all of the stress is being transmitted through the fluid phase, but once the particles begin to move, the particles bear the majority of the stress.

As the fluid begins to transmit the stress throughout the system, the particles begin to move and dilate, which can be seen by the increase in normal stress. The normal stress exhibits fluctuations because of random instabilities when some particles come in and out of contact with the wall. The stress on the moving wall from each phase was calculated by taking the normal and shear forces of the respective phases and dividing by the surface area of the wall. For the DEM, this force was the sum of all forces exerted by the particles in contact with the wall, and for the LBM, this force was the total hydrodynamic force exerted by the fluid to the wall as calculated by Equation 19. From Figure 9, the final value for total shear stress balances the applied stress of 10 Pa, and the final normal stress is approximately double the applied shear stress. The horizontal velocity profile of the particles is visualized in Figure 10.

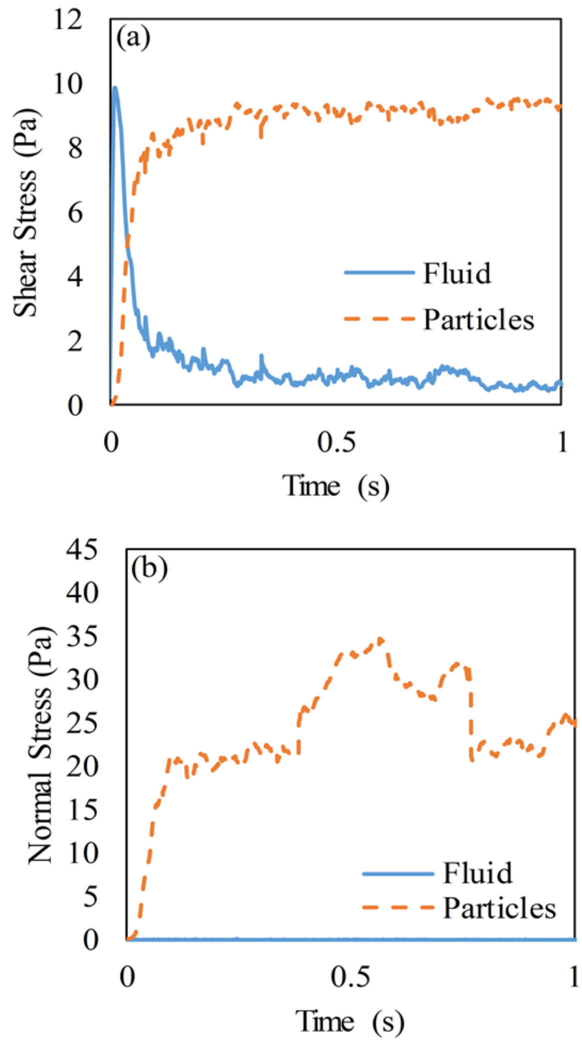

Figure 9. a) Shear stress plots for an applied wall stress of 10 Pa. b) Normal stress plots for an applied stress of 10 Pa. The normal stress due to the fluid's contribution was zero for the entire simulation. The stresses shown represent the wall exerting the stress onto the system, which is balanced by a reaction forces exerted by both fluid and particles on the wall.

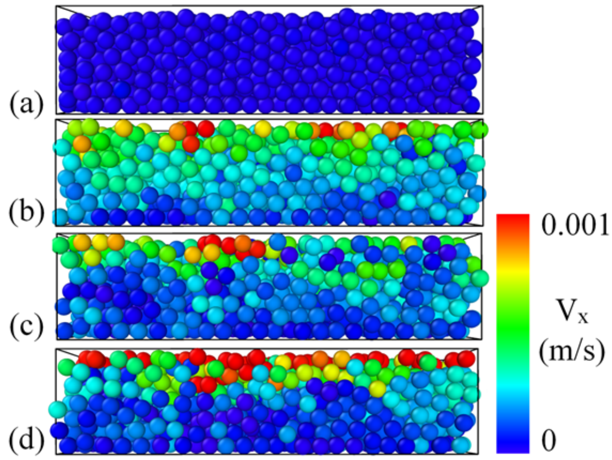

Figure 10. Visualization showing the particles at time step of a) 0.0s, b) 0.5s, c) 0.75s, and d) 1.5s for an applied stress of 10 Pa. The color corresponds to the particle velocity in the horizontal direction with the range based on the average plate velocity for 10 Pa.

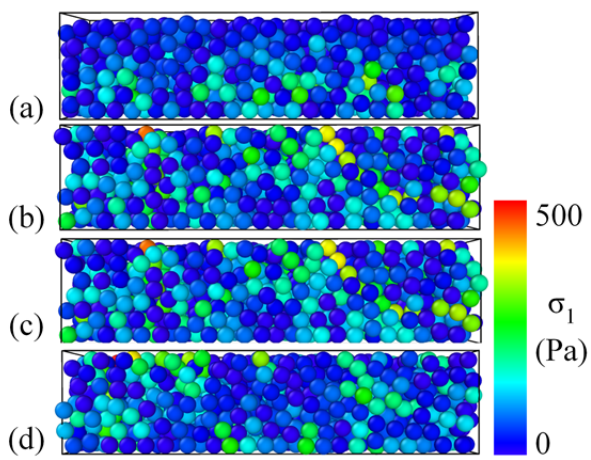

Figure 11. Visualization showing maximum compressive stress of each particle for a)0.0s b)0.5s c)0.75s and d)1.5s.

Figure 10 demonstrates all stages of the shear thickening. Starting in the settled initial configuration at 0 s, the particles are not in contact with the top plate. Once the hydrodynamic stress becomes large enough to move the particles, the particles displace into the void space near the top plate. Once the particles fill the top void space, the particles begin to resist the motion of the plate and begin to jam as seen in Figure 10b. For this applied shear stress, the hydrodynamic stresses are large enough to overcome the inter-particle stresses and move the particles closest to the moving wall, Figure 10c. Because the particles are displaced, more voids are created throughout the system, and gravity forces the particles to fill the voids [3].

To demonstrate the effect of particle contacts, a configuration of the particles at 0s, 0.5s, 0.75s, and 1.0s of simulated time is shown in Figure 11. Each particle is assigned a color corresponding to the maximum (principal) compressive particle stress as computed from the contact forces. The formation of force chains is evident where the higher stresses are concentrated in a chain like formation surrounded by “observer” particles with relatively small compressive stress. The stress history of the simulations is shown by plotting the stresses *p* and *q*, calculated by Eqs. 6 and 7, as seen in Figure 12. Also, to compare with Figures 10 and 11, the stress path for an applied stress of 10 Pa is shown in Figure 13.

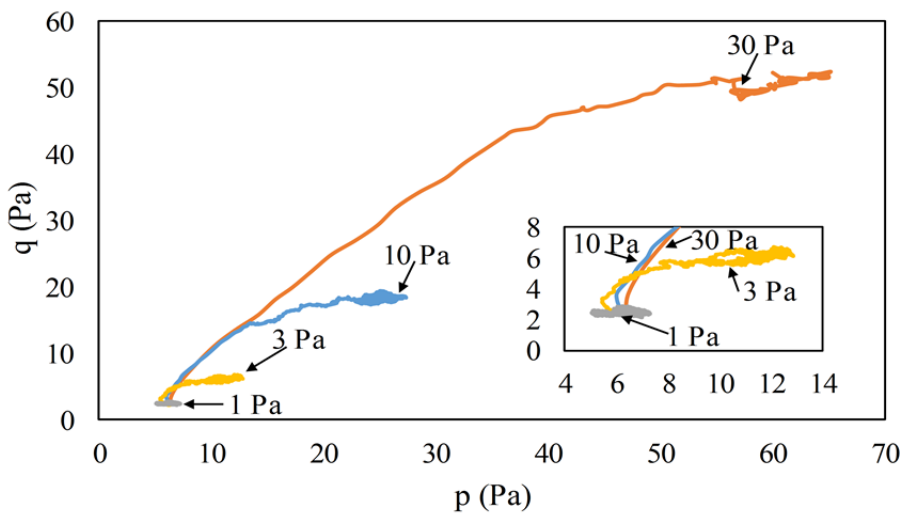

Figure 12. Stress path plots for different values of applied shear stress. The inset plot magnifies q values in the low stress range.

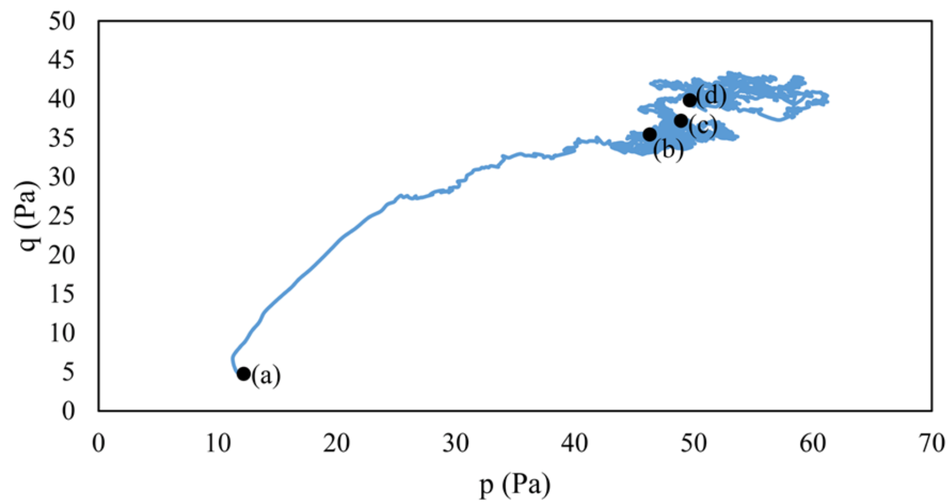

Figure 13. Stress path plot for an applied stress of 10 Pa. The black dots represent the stresses at times a) 0.0s, b) 0.5s, c) 0.75s, and d) 1.0s.

4. Parametric Studies

The DEM-LBM model was shown to yield realistic results in the previous section, thus providing a tool to further explore the DST phenomenon further through a parametric study. The purpose of this parametric study was to address particular issues that are difficult to determine from the existing DST experimental data. Whereas the experimental data provides great insight into DST, some aspects still remain unclear since certain measurements are not or cannot be made during the experimental tests. Most notably, the DEM-LBM model can separate the liquid and solid phase contributions to stress. It can provide detailed force-displacement micromechanical data which cannot be measured in experiments. Further, compared to alternative numerical models (e.g., Fernandez et al. 2013, Seto et al., 2014), the DEM-LBM model can properly deal with situations where particles settle at low stress due to high density of solid phase. In addition, the importance of some parameters was not anticipated at the time. The advantage of realistic numerical simulations is that quantities difficult to measure experimentally can be determined at high resolution by simulation, thus permitting better understanding of physical mechanisms involved. The following sections present simulation results and discuss the DEM-LBM model response for different soil fraction, particle-wall contact stiffness and particle friction. The model described in the previous section was used as a reference. Each parameter of interest was varied while the remaining parameters were kept constant.

4.1. Solid fraction

The first parameter studied was the solid fraction of particles in the system. Since this parameter represents the number of particles or the amount of solid present, the system will behave more like a solid with increasing solid fraction. Since the Reynolds number is so low, the particle fraction of 0.0, fluid only, shows Newtonian behavior, which is the assumption in the DEM-LBM model. Since the initial system had a solid fraction of 0.53, the values of 0.45 and 0.3 were chosen to show the lower limit and an intermediate value.

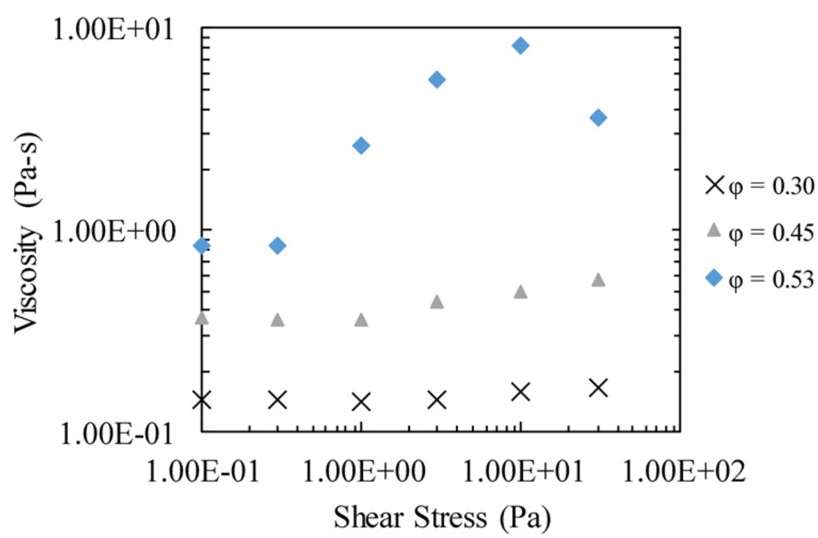

Figure 14. Viscosity versus shear stress plot for different values of solid fraction

Figure 14 shows a dependence of calculated viscosity values on the applied shear stress for solid fractions of 0.3, 0.45, and 0.53. For a fixed distance between the rotating plates, increasing the number of particles increases the solid fraction and presumably the amount of shear thickening. From Figure 14, the higher the solid fraction, the more particles are involved, and the more stress can be transmitted throughout the system. Also, at the low solid fraction values, only marginal shear thickening is observed, which agrees with experimental data.

4.2. Particle-Wall Contact Stiffness

To increase the maximum value of applied shear stress that exhibits shear thickening, either the boundary stiffness or equivalently, the confining pressure must be increased. Brown and Jaeger [3] showed that increasing the stiffness of the confining walls in their experiments increased the maximum shear stress range. For the DEM-LBM model developed in the current study, the viscosity of the system at higher applied stresses was increased by increasing the stiffness parameter that governs the contact between wall and particle, consequently increasing the shear thickening stress range.

The initial value of the wall stiffness was 0.5 N/m. The small values of wall-particle stiffness used in the DEM-LBM can be attributed to the fact that the experiment setup has a solid fluid interaction boundary. To see the effects of changing the wall stiffness, values of 0.25 and 1.0 N/m were applied. The results are shown in Figure 15. By decreasing the stiffness from 0.5 to 0.25 N/m, the maximum value for viscosity is noticeably decreased and seems to occur at lower values of applied shear stress. The system with lower wall stiffness shows the transition between shear thickening and thinning occurs between 3 and 10 Pa., which is earlier than the system with original wall stiffness value of 0.5 N/m. By increasing the wall stiffness to 1.0 N/m, the viscosity-stress curve shows little change, except at the final value of applied stress of 30 Pa, where the amount of shear thinning is reduced. The extension of the stress zone that shows shear thickening becomes most evident when the wall stiffness was increased to a value of 10.0 N/m for which the system shows shear thickening even at the applied stress of 30 Pa, where no other boundary stiffness exhibits thickening. From these data, the wall-particle stiffness parameter in the DEM-LBM model seems to control the maximum applied shear stress that induces shear thickening, but this parameter does not increase viscosity of the system beyond a certain applied shear stress threshold, which agrees with Brown and Jaeger's [3] observations.

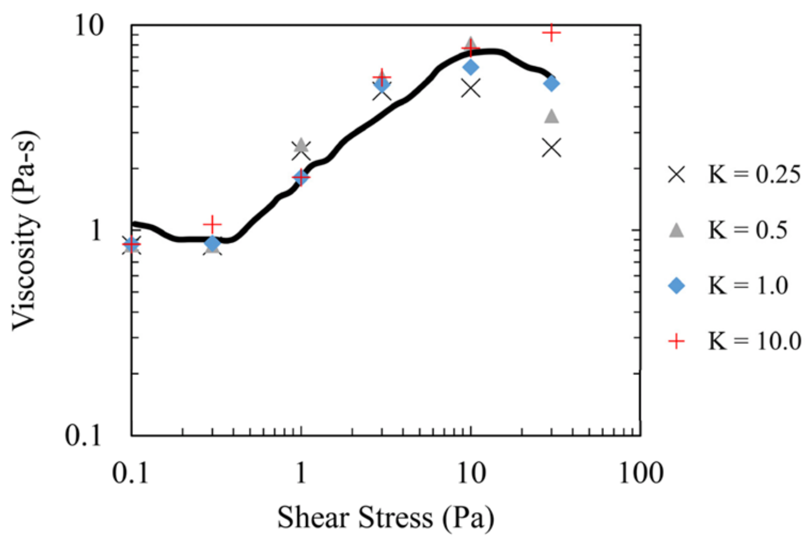

Figure 15. Viscosity versus shear stress plot for parametric study of wall-particles stiffness.

4.3. Particle Friction

The friction from the inter-particle interactions determines the ability to maintain force chains when the system is subjected to shear loading. Initially, the value of 0.8 was applied. This value was chosen as the maximum value, and the values of 0.25 and 0.5 were examined in addition. New initial configurations were created to account for the differences in settling due to changes in particle friction.

The results of changing the inter-particle friction parameter can be seen in Figure 16. The general behavior of the viscosity-stress curves displayed similar trends for all friction values, although the maximum value of viscosity was greatly decreased with decreasing friction. The expectations for this parameter study were that once the friction coefficient was reduced sufficiently, the particle-fluid solution would collapse. From Figure 16, as the friction parameter is increased from 0.25 to 0.5, the curves seem to be approaching the values at 0.8 Also, as the friction decreases, the system begins to behave like a Newtonian fluid – showing little shear thickening for this range of applied shear stress [4,9].

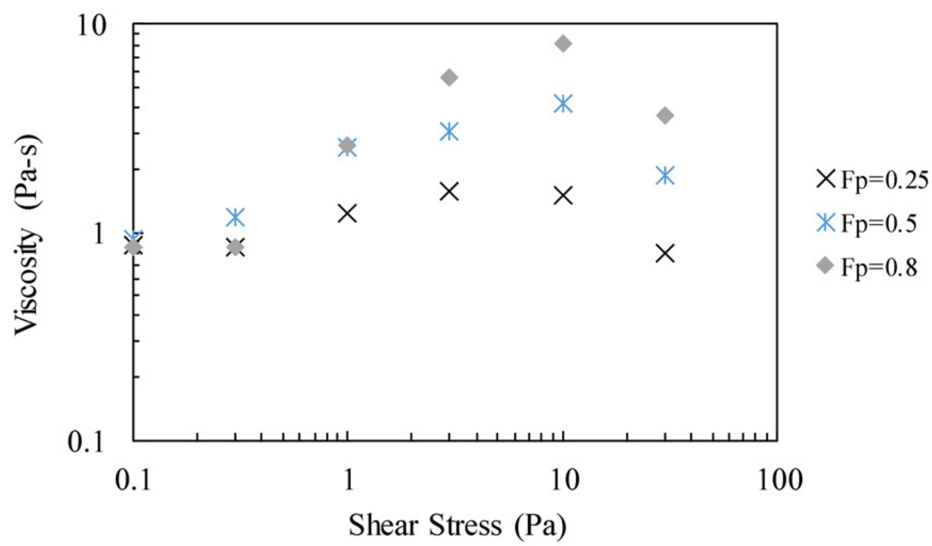

Figure 16. Viscosity versus shear stress plot for different values of inter-particle friction coefficient (Fp).

5. Discussion

Motivation for this study arose from previous cases in geomechanics where the DEM was used to model an experiment where dilation was a key phenomenon (e.g., Peters and Walizer, 2013). Since the dilation phenomenon has been a focus in descriptions of shear thickening fluid, the current DEM-LBM model proved to be a good fit for this type of simulation. The DEM-LBM model that was developed in this study provides a robust tool to determine the forces being exerted by the fluid phase and the solid phases separately, a feature that is not feasible in an experimental setup.

As expected in the shear thickening simulations, the fluid and solid phases have different roles in contributing to DST. At the low end of the applied stress range, the hydrodynamic stresses are not large enough to even move the particles, and the fluid contributes all of the resistance in the system. However, when the hydrodynamic stresses become large enough to move the particles, the inter-particle friction forces dominate the system's resistance, as seen in Figure 9. For the shear thickening to occur, the confining boundary stresses must be larger than these inter-particle stresses. Therefore, the role of the LBM fluid phase is to carry the stresses through the particles, and the role of the DEM particles is to transfer forces through the solid phase once sufficient dilation has occurred.

Since Brown and Jaeger [3] reported large differences in viscosity for different loading durations, the particle velocities for the DEM-LBM model were compared to the experimental results. In the region to the left of the dashed line in Figure 7, the DEM-LBM model captures the abrupt change in the velocity profile. The step-like layering can also be observed in the bulk region, region to the right of the dashed line, but the layering is not as pronounced as the experimental data. For the applied stresses of 1 Pa, 3 Pa, and 10 Pa, the DEM-LBM data was directly compared to the velocity profiles generated by Brown and Jaeger [3]. The model's results show overall good agreement to the experimental data, but some slight differences can be observed. For example in Figure 8.c, the model does not quite capture the discontinuity as quickly as the experimental method. These differences could be explained by the different loading conditions and by the methods used for measuring the average particle velocity.

As Brown and Jaeger [3] discussed, dilation seems to accompany the shear thickening. To interpret the role of friction we consider the intergranular stress, where intergranular implies that component of total stress transferred through solid-on-solid contacts between particles. From inspection of the simulated stress paths, as the particle mass is sheared, the fluid pressure drops causing an increase in intergranular stress. Thus the particle mass is stiffened. Whether dilation is a sufficient, necessary, or merely attendant condition is an open question. The geomechanical dilation has already been successfully simulated with the DEM under imposed constant-volume constraint (Peters *et al.* 2013), and appears to be important in the shear thickening behavior as well. As seen in Figures 10 and 11, the DEM-LBM model allows the particles to dilate when sufficient stress is applied. At the beginning of the simulations, the particles are settled. Throughout the simulation, the particles displace and expand the volume according to geometric constraints and the applied stresses. An interesting picture emerges from the average solid stress state, as shown in Figure 12, where the stresses p and q are plotted. The relationship between p and q follows that found for dilatant soils in undrained triaxial shear tests in soil mechanics. The degree to which the intergranular stress p increases depends on the applied shear stress. It appears that this increase in p occurs early as the particles are engaging the plate.

As shown in the parametric study, a number of parameters affect the amount of shear thickening that occurs in the simulations:

- First, the solid fraction effects on the intensity of shear thickening were examined. Below certain solid fraction, the system shows no shear thickening. The trend from the DEM-LBM model, seen in Figure 14, matches the behavior seen in the experimental data by Brown and Jaeger [3].

- Second, the effect of the stiffness of the wall-particle interaction on the range of the applied stress where shear thickening occurs was evaluated. Brown and Jaeger [3] reported a linear dependence between the confining stiffness and the maximum shear thickening stress. From Figure 15, the DEM-LBM model shows that increasing the wall-particle stiffness for the confining walls shifted the viscosity-stress curves. Changing the wall-particle contact stiffness did not increase the viscosity of the system, but it did change the stress scale. Although the particular values chosen for the DEM-LBM wall stiffness were much lower than that of a typical parallel plate setup with metal plates on the boundary, the wall stiffness values were a better match for the values for boundary stiffness related to the confining effects due to surface tension [3]. Therefore, the DEM-LBM model matches the experimental data by the DEM-LBM effectively matching the softer boundary condition. Interestingly, the viscosity curves vary significantly when the applied stress values are greater than 10 Pa. By increasing K, the maximum shear stress for shear thickening was increased. Therefore, the systems with the lower K show shear thinning above the 10 Pa applied stress, while the systems with the higher values of K show shear thickening. This change from shear thinning to shear thickening causes the large differences for stresses above 10 Pa.
- Third, the effects of friction coefficient governing inter-particle contacts on the amount of shear thickening were analyzed. For the DEM-LMB model, increasing the friction between particles increased the total amount of shear thickening but did not affect the range of stresses where shear thickening was observed. As the friction decreased, the system approached Newtonian fluid behavior.

The current version of the DEM-LBM model is limited to low Reynolds number flows for larger particles, where the Brownian forces are negligible. By eliminating the inertial and size effects, the effects of dilation, inter-particles stresses, and boundary confinement were the focus of this study. However, the DEM-LBM model could be modified to accommodate high Reynolds number flows, where inertial effects would be present in the fluid phase, and small-particle suspensions, where Brownian forces would be present (see Yeoh et al. 2013). The current study dealt with situations where particles settle at low stress. It is noted that further research is needed to assess the performance of the DEM-LBM model for simulating cases where the lubrication forces are expected to dominate. Further, while beyond the scope of the current study, it is worthy to use the DEM-LBM model in future research in an attempt to numerically simulate shear thickening of the soil-fluid mixture in the absence of gravity. The presented DEM-LBM modeling effort was carried out in the presence of gravity. One may argue that the strong influence of gravity in such a system results in a segregated flow at low shear rate or shear stress, and a well-mixed state due to resuspensions at high shear rate.

6. Summary and Conclusions

By coupling the discrete element method (DEM) and lattice Boltzmann method (LBM), the phenomenon of shear thickening in particle suspensions was successfully modeled. The results of the DEM-LBM model were shown to be realistic by comparing with experimental data for spherical glass particles immersed in oil. By keeping the Reynolds number low and particle sizes in an appropriate range, inertial effects and size effects were minimized. With this criteria, the major contributions to the stresses involved were gravitational, viscous, and inter-particles, which could all be modeled by the DEM-LBM. From previous studies, the mechanisms involved are the same as those commonly observed in geotechnical strength tests.

Parameters such as solid fraction, wall-particle stiffness, and the particle friction coefficient were studied. From the parameter study, the DEM-LBM model results, with calibrated parameters, agree with the expected outcomes when the key parameters are varied. For example, by decreasing the amount of particles in the initial DEM-LBM system, the solid fraction was decreased, resulting in less significant increase of the viscosity. The study of the solid fraction showed that the DST only occurs for a certain range of solid fractions. Next, the variation of the wall-particle stiffness parameter in the DEM showed that the range of shear stress in which shear thickening occurs could be extended by increasing the wall stiffness, or boundary confinement. Previous simulations have shown the effects of particle friction and solid fraction, but the DEM-LBM model presents a new result showing that increasing boundary stiffness directly increases the shear stress that onsets shear thickening. The inter-particle friction parameter illustrated that the resistance of the global system depends on the resistance of the local particles, with lower particle friction lowering the global resistance.

By evaluating the DEM-LBM model with the experimental data provided, this paper presents a model that can simulate the shear-thickening phenomenon and help understand the mechanisms that cause shear thickening. For example, this model can calculate the individual contribution of both the solid phase and the fluid phase, which is not possible in the experiment. Also, this paper shows how the DEM-LBM model could be useful in other applications of densely packed suspensions where dilation occurs.

Acknowledgements

This effort was sponsored by the Engineering Research & Development Center under Cooperative Agreement number W912HZ-15-2-0004. The views and conclusions contained herein are those of the authors and should not be interpreted as necessarily representing the official policies or endorsements, either expressed or implied, of the Engineering Research & Development Center or the U.S. Government. This paper is based on the work conducted under Task 12: Mobility Modeling for Soils. Roger King, Director of the Center for Advanced Vehicular Systems (CAVS) at Mississippi State University, was principal investigator for W912HZ-15-2-0004 and Farshid Vahedifard was the lead for Task 12.

References

[1] Barnes, H. A. "Shear-thickening ("Dilatancy") in suspensions of nonaggregating solid particles dispersed in Newtonian liquids." *Journal of Rheology* (1978-present) 33.2 (1989): 329-366.

[2] Wagner, N. J., and J.F. Brady. "Shear thickening in colloidal dispersions." *Physics Today* 62.10 (2009): 27-32.

[3] Brown, E., and H. M. Jaeger. "The role of dilation and confining stresses in shear thickening of dense suspensions." *Journal of Rheology (1978-present)* 56.4, 875-923 (2012).

[4] Fernandez, N., R. Mani, D. Rinaldi, D. Kadau, M. Mosquet, H. Lombois-Burger, and L. Isa. "Microscopic mechanism for shear thickening of non-Brownian suspensions." *Physical Review Letters* 111.10, 108301 (2013).

[5] Seto, R., R. Mari, J. F. Morris, and M. M. Denn. "Discontinuous shear thickening of frictional hard-sphere suspensions." *Physical Review Letters*, *111*(21), 218301 (2013).

[6] Heussinger, C. "Shear thickening in granular suspensions: Interparticle friction and dynamically correlated clusters." *PhysicalRreview E*, *88*(5), 050201 (2013).

[7] Brown, E., and H. M. Jaeger. "Shear thickening in concentrated suspensions: phenomenology, mechanisms and relations to jamming. "*Reports on Progress in Physics* 77.4, 046602 (2014).

[8] Wyart, M., and M. E. Cates. "Discontinuous shear thickening without inertia in dense non-Brownian suspensions." *Physical Review Letters* 112.9 098302 (2014).

[9] Mari, R., R. Seto, J. F. Morris, and M. M. Denn. "Discontinuous shear thickening in Brownian suspensions by dynamic simulation." *Proceedings of the National Academy of Sciences*, *112*(50), 15326-15330 (2015).

[10] Lee, Y. S., E. D. Wetzel, and N. J. Wagner. "The ballistic impact characteristics of Kevlar® woven fabrics impregnated with a colloidal shear thickening fluid." *Journal of Materials Science* 38.13, 2825-2833 (2003).

[11] Brown, E., N. A. Forman, C. S. Orellana, H. Zhang, B. W. Maynor, D. E. Betts, J. M. DeSimone, and H. M. Jaeger. "Generality of shear thickening in dense suspensions." *Nature Materials*, *9*(3), 220- 224, (2010).

[12] Nazockdast, E., and J. F. Morris. "Microstructural theory and the rheology of concentrated colloidal suspensions." *Journal of Fluid Mechanics* 713, 420-452 (2012).

[13] Jiang, W., S. Xuan, and X. Gong. "The role of shear in the transition from continuous shear thickening to discontinuous shear thickening." *Applied Physics Letters* 106.15, 151902 (2015).

[14] Peters, I. R., S. Majumdar, and H. M. Jaeger. “Direct observation of dynamic shear jamming in dense suspensions.” *Nature*, *532*(7598), 214-217 (2016).

[15] Brown, E., and H. M. Jaeger. "Dynamic jamming point for shear thickening suspensions." *Physical Review Letters* 103.8, 086001 (2009).

[16] Maranzano, B. J., and N. J. Wagner. "The effects of interparticle interactions and particle size on reversible shear thickening: Hard-sphere colloidal dispersions." *Journal of Rheology (1978-present)* 45.5, 1205-1222 (2001).

[17] Peters, J. F., M. Muthuswamy, J. Wibowo, and A. Tordesillas. "Characterization of force chains in granular material." *Physical Review E*, *72*(4), 041307 (2005).

[18] Tordesillas, A., S. Pucilowski, D. M. Walker, J. Peters, and M. Hopkins. "*A complex network analysis of granular fabric evolution in three-dimensions*." Melbourne University Victoria (Australia) (2011).

[19] Cates, M. E., J. P. Wittmer, J. P. Bouchaud, and P. Claudin. "Jamming, force chains, and fragile matter." *Physical Review Letters*, *81*(9), 1841, (1998).

[20] Nott, P. R., and J. F. Brady. "Pressure-driven flow of suspensions: simulation and theory." *Journal of Fluid Mechanics* 275, 157-199 (1994).

[21] Bian, X., S. Litvinov, M. Ellero, and N. J. Wagner. "Hydrodynamic shear thickening of particulate suspension under confinement." *Journal of Non-Newtonian Fluid Mechanics*, *213*, 39-49 (2014).

[22] Ness, C., and J. Sun. "Shear thickening regimes of dense non-Brownian suspensions." *Soft Matter*, 12, 914-924 (2016).

[23] Feng, Y. T., K. Han, and D. R. J. Owen. "Combined three-dimensional lattice Boltzmann method and discrete element method for modelling fluid–particle interactions with experimental assessment." *International Journal for Numerical Methods in Engineering* 81.2, 229-245 (2010).

[24] Lominé, F., L. Scholtès, L. Sibille, and P. Poullain. "Modeling of fluid–solid interaction in granular media with coupled lattice Boltzmann/discrete element methods: application to

piping erosion." *International Journal for Numerical and Analytical Methods in Geomechanics*, *37*(6), 577-596, (2013).

[25] Sun, W. C., M. R. Kuhn, and J. W. Rudnicki. "A multiscale DEM-LBM analysis on permeability evolutions inside a dilatant shear band." *Acta Geotech* 8(5):465–480 (2013).

[26] Han, Y., and P. A. Cundall. "LBM–DEM modeling of fluid–solid interaction in porous media." *International Journal for Numerical and Analytical Methods in Geomechanics* 37.10, 1391-1407 (2013).

[27] Jelinek, B., M. Eshraghi, S. D. Felicelli, and J. F. Peters. "Large-scale Parallel Lattice Boltzmann - Cellular Automaton Model of Two-dimensional Dendritic Growth." *Computer Physics Communications*. Elsevier. *185*(3), 939-947, (2013).

[28] Cundall P.A., and O. D. L. Strack. "A discrete numerical model for granular assemblies." *Geotechnique* 29.1, 47-65 (1979).

[29] Cole, D. M., and J. F. Peters. "Grain-scale mechanics of geologic materials and lunar simulants under normal loading." *Granular Matter* 10.3, 171-185 (2008).

[30] Owen, D. R. J., C. R. Leonardi, and Y. T. Feng. "An efficient framework for fluid–structure interaction using the lattice Boltzmann method and immersed moving boundaries." *International Journal for Numerical Methods in Engineering* 87.1-5, 66-95 (2011).

[31] Succi, S. *The lattice Boltzmann equation: for fluid dynamics and beyond*. Oxford University Press, 2001.

[32] Rothman, D. H., and S. Zaleski. *Lattice-gas cellular automata: simple models of complex hydrodynamics* (Vol. 5). Cambridge University Press, 2004.

[33] Sukop, M. C. “Thorne, D. T. Lattice Boltzmann modeling: An introduction for geoscientists and engineers.” Springer, 2006.

[34] Boltzmann L. *Weitere Studien über das Wärmegleichgewicht unter Gas-molekülen. Wissenschaftliche Abhandlungen*, 1:316–402 (1872).

[35] Chapman S, and T. G. Cowling. *The Mathematical Theory of Non-uniform Gases: An Account of the Kinetic Theory of Viscosity, Thermal Conduction and Diffusion in Gases* (Cambridge Mathematical Library). Cambridge University Press: Cambridge, New York, Melbourne, 1991.

[36] Bhatnagar, P. L., E. P. Gross, and M. Krook. "A model for collision processes in gases. I. Small amplitude processes in charged and neutral one-component systems." *Physical Review* 94.3, 511 (1954).

[37] Qian, Y. H., D. d'Humières, and P. Lallemand. "Lattice BGK models for Navier-Stokes equation." *EPL (Europhysics Letters)*, *17*(6), 479 (1992).

[38] Chapman, S., and T. G. Cowling. *The mathematical theory of non-uniform gases: an account of the kinetic theory of viscosity, thermal conduction and diffusion in gases*. Cambridge university press, 1970.

[39] Noble, D. R., and J. R. Torczynski. "A lattice-Boltzmann method for partially saturated computational cells." *International Journal of Modern Physics C*9.08, 1189-1201 (1998).

[40] Strack, O. E., and B. K. Cook. "Three-dimensional immersed boundary conditions for moving solids in the lattice-Boltzmann method." *International Journal for Numerical Methods in Fluids*, *55*(2), 103 (2007).

[41] Feng, Z. G., and E. E. Michaelides. "The immersed boundary-lattice Boltzmann method for solving fluid–particles interaction problems." *Journal of Computational Physics* 195.2 (2004): 602-628.

List of Figures

Figure 15. Viscosity versus shear stress plot for parametric study of wall-particles stiffness.

Figure 16. Viscosity versus shear stress plot for different values of inter-particle friction coefficient (Fp).

List of Tables